

IMAGING OF ELEMENT EXCITATIONS WITH SPHERICAL SCANNING

Doren W. Hess

dhess@mi-technologies.com

Scott T. McBride

smcbride@mi-technologies.com

MI Technologies

1125 Satellite Blvd, Suite 100, Suwanee, GA 30024

ABSTRACT

We review two conventional algorithms for aperture back-projection from spherical near-field data, with the goal of quantifying array-element excitations. The first algorithm produces that portion of the near field that radiates to the far field. The second algorithm divides out the element pattern prior to the transformation, and produces an estimate of the element excitations. We introduce a variation of this element-excitation algorithm that, for some arrays, can improve the fidelity of this conventional estimate. We apply the three algorithms to measured data, where the algorithms' assumptions are tested, and to synthesized data, where the expected results are known exactly. For the array geometries measured and simulated, this new algorithm shows dramatic improvement.

Two of the three algorithms require an estimate of the element pattern, which they assume to be common to all the elements. We describe our measurement of our array's element pattern, as well as the use of the *IsoFilter*[™] to center the element pattern and limit the edge effects.

Keywords: Aperture Back-Projection Imaging, Element Diagnostics, Spherical Near-Field Scanning, Phased Array Testing.

1.0 Introduction

The testing of a phased-array antenna usually includes calibrating the complex excitations of the various elements for different commanded beam states. Two aperture back-projection methods are commonly used to assist in this calibration, with one algorithm yielding the portion of the aperture's near field that radiates to the far field, and the other yielding an estimate of the individual element excitations. Unfortunately, the fidelity of each technique often falls short of the calibration requirements.

Our interest in this problem was stimulated by our curiosity regarding a fixed flat plate slotted waveguide array that we have on hand here at MI Technologies. Measurements of the far-field pattern of the array and the

element pattern were carried out using spherical near-field scanning on several different ranges and under differing conditions. Consistent results have been obtained and published showing that back-projection to obtain the aperture field is a robust and stable process using spherical near-field scanning [1]. However, the limitations of resolution have made the results unsatisfying and we therefore have investigated further the question of how to resolve, unambiguously and uniquely, the excitations of individual elements.

The original goal of this paper was to compare the results of these two conventional back-projection algorithms, and to experiment with techniques for measuring a single embedded element's pattern. During these efforts, we discovered a straightforward enhancement to the conventional element-excitation algorithm that, for arrays with elements spaced at more than $\lambda/2$, dramatically improves its estimate's accuracy. We have included this enhancement as a third back-projection algorithm for comparison.

In Section 2, we very briefly show the mathematics involved in the conventional back-projection to radiating aperture field. This information is presented in order to illustrate the subtle contrast to the conventional element-excitation algorithm.

In Section 3, we discuss at a high level the mathematics behind both the conventional and the enhanced element-excitation algorithms to show their differences, and also to describe the element-excitation enhancement.

In Section 4, we describe measurements we made on our slotted array with two elements intentionally blocked. We then do a qualitative comparison of this array's back-projection results from each of the three methods. The two element-excitation algorithms discussed in Section 3 require an element pattern that will be considered common to all the array elements. Measurement of the element pattern for a fixed phased array, given only that array, has been a problem without a good answer. The reason is that any attempt to isolate an embedded element has a high probability of disturbing the pattern one is attempting to measure. Section 4 discusses our

measurement of the element pattern, and shows the means we have employed to address that difficulty by use of the recently devised technique we have termed *IsoFilter*TM.

In Section 5, we quantify the accuracy of each algorithm. We do this by synthesizing an array with known excitations and element pattern, and comparing the excitation estimates from the three algorithms to those known values.

2. Computing Radiating Aperture Field

Back-projection to an aperture with near-field scanning has been thoroughly explored. Its application to phased-array element alignment and element diagnostics has found considerable success. [2] -[12] Back-projection using spherical near-field scanning data has two advantages: First, the reduced presence of the standing wave between the array antenna and the near-field probe; and second, the greater aperture resolution due to the lack of any scan-area truncation.

We have in the past reported on two mathematically equivalent theoretical approaches for back-projection. [1] An algorithm based upon these approaches is described by the following pair of equations:

$$E_{x'}^{Aperture} \propto \mathfrak{F}^{-1} \left[E_{\theta'} \cos \phi' - \frac{E_{\phi'}}{\cos \theta'} \sin \phi' \right] \quad (1a)$$

$$E_{y'}^{Aperture} \propto \mathfrak{F}^{-1} \left[E_{\theta'} \sin \phi' - \frac{E_{\phi'}}{\cos \theta'} \cos \phi' \right] \quad (1b)$$

These yield the radiating aperture field from the far field.

3. Element-Excitation Algorithm

For an array antenna, the near electric field may be less interesting than the discrete set of element excitations. If we form an array with several identical elements that have complex excitations V_i and common pattern $P(\mathbf{K})$, then the array's far-field pattern $E(\mathbf{K})$ will be given by the first form of equation (2).

$$\begin{aligned} \vec{E}(\vec{K}) &= \vec{P}(\vec{K}) \sum V_i e^{-j\vec{K} \cdot \vec{R}_i} \\ \vec{P}(\vec{K})^\times \cdot \vec{E}(\vec{K}) &= [\vec{P}(\vec{K})^\times \cdot \vec{P}(\vec{K})] \sum V_i e^{-j\vec{K} \cdot \vec{R}_i} \\ \frac{\vec{P}(\vec{K})^\times \cdot \vec{E}(\vec{K})}{\vec{P}(\vec{K})^\times \cdot \vec{P}(\vec{K})} &= \sum V_i e^{-j\vec{K} \cdot \vec{R}_i} \end{aligned} \quad (2)$$

where

- \mathbf{K} is the direction vector in the spectral domain
- $E(\mathbf{K})$ is the array's far electric field
- $P(\mathbf{K})$ is the far-field pattern of a centered element, assumed here to be equal for all elements
- V_i is the complex excitation of the i^{th} element (our desired result)

\mathbf{R}_i is the location of the i^{th} element in the aperture

The summation Σ occurs over the set of elements

$[\vec{P}(\vec{K})^\times \cdot \vec{P}(\vec{K})]$ is the element radiation intensity

\times is the complex conjugate operator

As it turns out, the inverse Fourier transform can be used to solve for the element excitations V_i at the known element locations \mathbf{R}_i . To see why this is so, it may be helpful here to review briefly a few basic properties of the Fourier transform [14]. These properties are normally written using time t and frequency ω as the two domains, so we will repeat the relevant properties in that form. In our equation (2) above, time t corresponds to position vector \mathbf{R} in the aperture domain, and frequency ω corresponds to the direction vector \mathbf{K} in the spectral domain. Extension to multiple dimensions is reasonably straightforward [13]. Part of that extension is that the quantity ωt is replaced with the dot product $\mathbf{K} \cdot \mathbf{R}$. Note that so far in this discussion, both time and frequency are continuous, not sampled.

$$\begin{aligned} f(t) &\Leftrightarrow F(e^{j\omega}), \quad g(t) \Leftrightarrow G(e^{j\omega}), \quad \delta(t - t_0) \Leftrightarrow e^{-j\omega t_0} \\ f(t) * g(t) &\Leftrightarrow F(e^{j\omega})G(e^{j\omega}) \\ f(t - t_0) &= f(t) * \delta(t - t_0) \Leftrightarrow F(e^{j\omega})e^{-j\omega t_0} \\ af(t) + bg(t) &\Leftrightarrow aF(e^{j\omega}) + bG(e^{j\omega}) \end{aligned} \quad (3)$$

where

- \Leftrightarrow is the Fourier transform operator
- δ is the impulse or Dirac delta function
- t_0 , a , and b are arbitrary constants
- $*$ is the convolution operator

We can easily combine the properties in (3) above to show the inverse continuous 3D Fourier transform of the summation in (2) above by inspection:

$$\sum A_i \delta(\vec{R} - \vec{R}_i) \Leftrightarrow \frac{\vec{P}(\vec{K})^\times \cdot \vec{E}(\vec{K})}{\vec{P}(\vec{K})^\times \cdot \vec{P}(\vec{K})} = \sum A_i e^{-j\vec{K} \cdot \vec{R}_i} \quad (4)$$

For elements in a plane, the transform collapses to 2D (with proper alignment of the basis vectors). Similarly, when the elements are in a line, the transform collapses to 1D. This discussion concentrates on the 2D case, with the elements in the X-Y plane.

Equation (4) above gives the incorrect impression that the result of an inverse FFT of the ratio will provide a train of impulses on output, with one impulse per element. The reason this does not happen is the truncation of the spectral domain (due to our lack of information) where $\| [K_x, K_y] \| > 2\pi/\lambda$. This truncation can be thought of as a windowing function $W(\mathbf{K})$ that is zero outside this boundary.

By default, $W(\mathbf{K})$ is the Circ function (=1 inside, =0 outside), which has the inverse transform of a Bessel function $w(\mathbf{R})=J_1(\alpha|\mathbf{R}|)/(\alpha|\mathbf{R}|)$ [2], which is circularly symmetric. This transform pair is shown graphically in Figure 1 below.

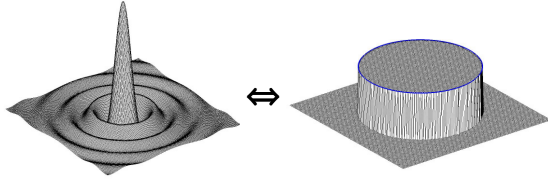


Figure 1.–Impulse Response -Uniform Circular Truncation

The convolution property in (3) shows that $w(\mathbf{R})$ will then be convolved with each of these elemental impulses. Since convolution with an impulse is merely a shift operation, each desired impulse in the spatial domain will be replaced with a weighted copy of the left-hand plot in Figure 1, shifted to be centered at that element location. The resulting distribution will be the sum of those weighted convolutions, $\sum V_i w(\mathbf{R}-\mathbf{R}_i)$.

The ability to quantify the excitations at the known element locations \mathbf{R}_i depends greatly on the value of $w(\mathbf{R}-\mathbf{R}_i)$ evaluated at the other element locations. For element k , for example, the error \mathcal{E} in the aperture image at $\mathbf{R}=\mathbf{R}_k$ is equal to

$$\mathcal{E}(\vec{\mathbf{R}}_k) = \sum_{i \neq k} V_i w(\vec{\mathbf{R}}_k - \vec{\mathbf{R}}_i) \quad (5)$$

There is a common misperception that the resolution of an aperture back-projection should be $\lambda/2$. If the K-space truncation were a square with $4\pi/\lambda$ on each side, then this would be the case. However, the region of K space that corresponds to real aspect angles has a circular outline with diameter equal to $4\pi/\lambda$. Since the circular truncation window is smaller than the square would be, the location of the lobe's first null in the spatial domain is further out than $\lambda/2$, at $|\mathbf{R}_i| = 0.61\lambda$ [2]. The second null occurs at 1.13λ , and subsequent nulls are evenly spaced about every 0.5λ relative to the second null. These null locations are shown in Figure 2 below. From the null spacings above, one can rapidly see that there is no element spacing that will drive the result of equation (5) above to zero. If we space our elements at 0.61λ , depicted by the vertical red lines in Figure 2, then the first null overlays the adjacent elements ($i=k\pm 1$), but there is still a significant contribution from $i=k\pm 2$, $i=k\pm 3$, and $i=k\pm 4$. To make matters worse, a 2D grid of elements will also have elements at radial distances in between the red lines shown. For arrays whose elements are spaced more than $\lambda/2$ apart, and certainly more than 0.707λ , there are some

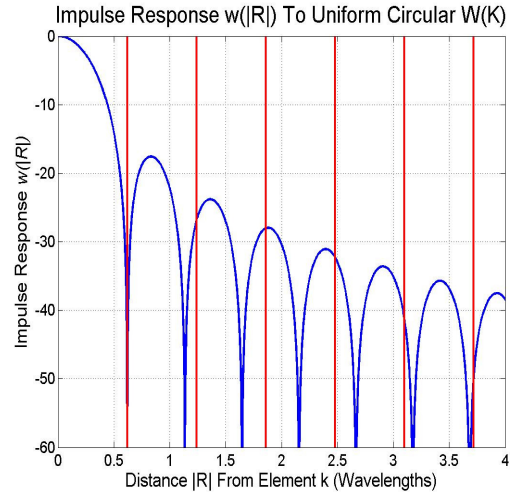


Figure 2. – Null Locations in Circ Function Transform

straightforward options for improving the accuracy of the element-excitation estimate. The key to this improvement is minimizing the sum in equation (5). The best way to do that, when possible, is to find a spectral truncation function $W(\mathbf{K})$ whose inverse transform $w(\mathbf{R})$ places nulls at all the other element locations. The only restriction on this $W(\mathbf{K})$ is that it must be zero for all $|\mathbf{K}| > 2\pi/\lambda$.

Our measured array is rectangularly packed, so our ideal $w(\mathbf{R})$ should have regularly spaced nulls on an X-Y grid. A uniform rectangular spectral window has these properties, and the width and height of the window controls the spacing between the nulls. Because our element spacing is 0.72λ ($>0.707\lambda$), the appropriate rectangular window can fit completely inside the $|\mathbf{K}|=2\pi/\lambda$ circle. We apply and compare this spectral window in the sections below.

Note that the true aperture-field computation discussed in Section 2 does not offer the option of altering the spectral truncation window $W(\mathbf{K})$. While doing so might help identify bad elements in an array, the resulting aperture distribution would represent neither radiating aperture field nor element excitation.

4. Measurements

In this Section we apply the three back-projection techniques to measured data. At MI Technologies we have measured a flat plate slotted array using spherical NF scanning. This 18-inch (45.7 cm) diameter array operates at frequencies near 9.375 GHz; it is linearly polarized and has first sidelobes that lie approximately 30 dB below the main beam peak. A photograph of this antenna is shown in Figure 3. For the purpose of this comparison, the two elements identified in Figure 3 were blocked with metalized tape. The three aperture distributions were evaluated first as 3D images, and then as 2D line cuts through a blocked element.

The two element-excitation algorithms we evaluated each require as input a far-field pattern that is assumed to be common to all elements. This average element pattern was obtained by a novel method that we describe.

The aperture-field back-projection was computed in a manner based upon straightforward application of Equation (1). To compute the element-excitation back-projections, the contribution of the element pattern to the plane wave spectrum was removed by dividing out the radiation intensity of the element as indicated in equation (2). The element excitations were computed using both the conventional approach, where $W(\mathbf{K})$ is always a uniform circle, and the enhanced approach, where for this array $W(\mathbf{K})$ is a uniform rectangle.

To measure the element pattern, all the elements of the array except one were blocked by use of metalized tape. The pattern of the single remaining unblocked element was then measured by spherical scanning.

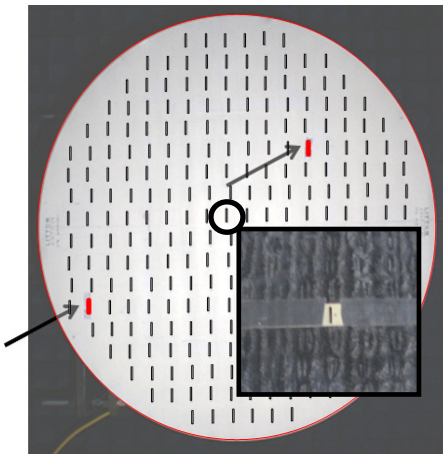


Figure 3. – Overlay of Element Map and Photograph of the 18 inch Flat Plate Array with the Blocked Elements Marked. Element Left Uncovered Shown by Circle and A Photo of it Appears in the Inset.

Because the unblocked element was not centered on the rotational center of the spherical scanner, to obtain an element pattern appropriately common to all the elements of the 18 inch array, a translation operation was carried out using *IsoFilter*TM. The translation feature has the effect of relocating the origin relative to the antenna, placing it at the position of the unblocked element. The *IsoFilter*TM technique has the additional advantage that modal filtering significantly improves the accuracy of the relative pattern, permitting the unimportant modes to be eliminated from consideration. The equatorial far-field pattern of the individual element is plotted over a hemisphere in

Figure 4. Notice that the pattern is very broad in the plane perpendicular to the axis of the slot and more narrow in

the plane containing the axis of the slot. The polarization is that of a magnetic dipole with its axis along the slot. It is well known that a slot behaves as a magnetic source, so this measured pattern is consistent with our expectation. Examination of a similar plot for the far-field phase shows a total variation of approximately 20 phase degrees.

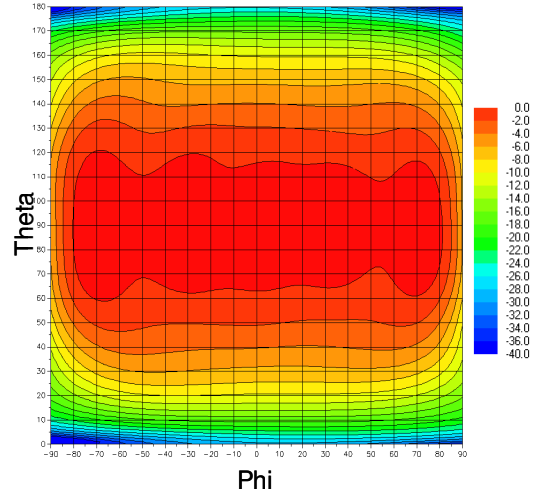


Figure 4. – Far-Field Pattern of Individual Element Measured with Spherical Near-Field Scanning

When this element pattern is used in conjunction with the far-field pattern from spherical near-field scanning, the element excitation image of Figure 5 results. This image is comparable to those published earlier. [1] We compare the difference between images formed from the aperture field and element excitation: We see in Figure 6 that when the amplitude is plotted along a line in the aperture passing through the blocked element, the element excitation function produced resolution similar to that of the aperture field. However, the 'hole' in the two conventional distributions contains a peak rather than the minimum amplitude we expect. This feature is brought about by the convolution of the resolution function $w(\mathbf{R})$ with the element excitations. It can be reduced by 'tuning' the window function $W(\mathbf{K})$, as discussed in Section 3, to place nulls in $w(\mathbf{R})$ at the X and Y element spacings. Figure 7 was produced by finding element excitations using this uniform rectangular window $W(\mathbf{K})$. Note how the distribution at the taped elements now forms deep nulls without a significant artificial peak, - Figures 6, 7.

5. Accuracy Assessment

While the imaging of measured data gives a qualitative comparison of the different diagnostic techniques, one cannot claim that one of these results is more accurate than the others. In order to do that, one must know what the correct answer is. To do that, we used synthesized data, where the element excitations and the common

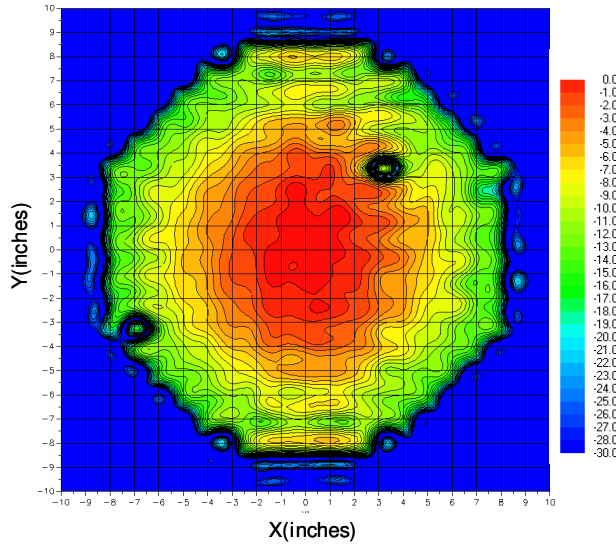


Figure 5. – Amplitude of Element Excitation Function Produced with Uniform Circular $W(K)$

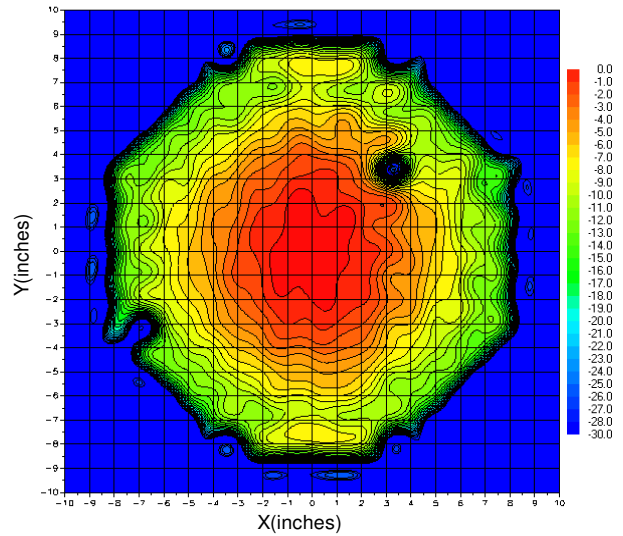


Figure 7. – Amplitude of Element Excitation Function Produced with Tuned $W(K)$

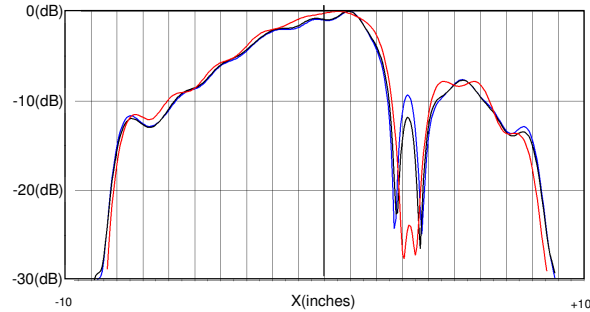


Figure 6. – Horizontal Amplitude Trace Through Taped Element

- Black:** Amplitude of Aperture Field
- Blue:** Amplitude of Element Excitation Function Produced with Uniform Weighting
- Red:** Amplitude of Element Excitation Function Produced with Tuned $W(K)$

element pattern are known exactly. Our model was a two-layer array of dipoles. The two layers were spaced in Z at $\lambda/4$, with one layer offset 90° in phase from the other to suppress the back lobe. These elemental dipole pairs were separated in X and Y by the same amount as the elements in our slotted array, about 0.72λ , to form a 21-by-21 array.

The element weights started as a simple Hanning function in X times a Hanning function in Y. Three of the elements then had their weights modified as follows:

- Element (15,15) set to -60 dB, 180°
- Element (5,8) offset +4.609 dB, $+10^\circ$
- Element (13,6) offset -1.549 dB, -5°

The model synthesized the response of a spherical near-field (SNF) probe to both the full array and to a single centered element. We then processed the SNF data to produce three aperture distributions:

1. Radiating aperture field
2. Element excitation with $W(K)$ = the Circ function
3. Element excitation with $W(K)$ tuned for ΔX and ΔY

The horizontal cuts through the -60 dB element are shown in Figure 8 below. Computing element excitation without tuning the spectral window provides a slight improvement over the radiating field estimate of the excitation. Only the element excitation with the tuned spectral window has removed the dimple at the location of the 'bad' element. Similarly, the horizontal cuts through the element with a 5° perturbation are shown in Figure 9 below.

The errors evaluated at the 'bad' element locations are shown in Table 1 below.

	Amplitude Errors			Phase Errors		
	Evaluation Method			Evaluation Method		
	1	2	3	1	2	3
Case	1	2	3	1	2	3
15, 15	53.0	49.0	1.3	0.4	0.0	0.4
5, 8	2.5	1.7	0.2	3.5	2.8	0.0
13, 6	1.4	1.1	0.1	6.2	3.9	0.0

To compare the accuracy over all the elements, we computed the cumulative density function (CDF) for each error distribution in both amplitude (in Figure 10) and phase (in Figure 11). These plots show the probability that the error's magnitude will be less than the value along the bottom of the plot.

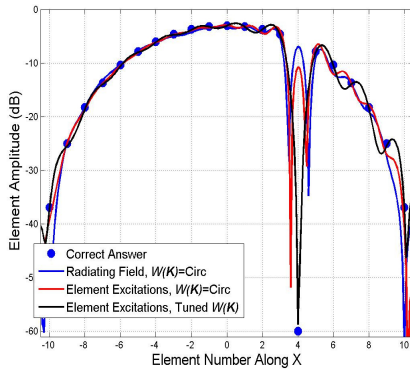


Figure 8 –Amplitude Accuracy Comparison

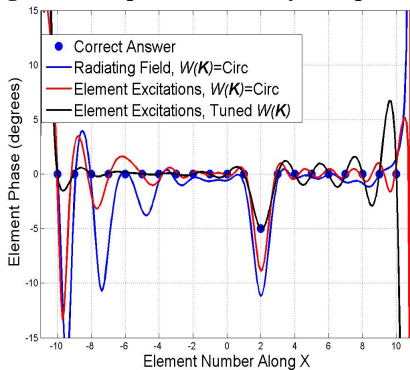


Figure 9 – Phase Accuracy Comparison

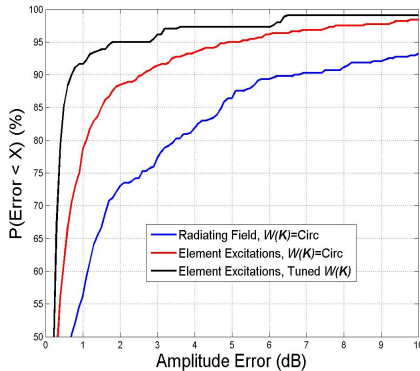


Figure 10 – Amplitude Error CDFs

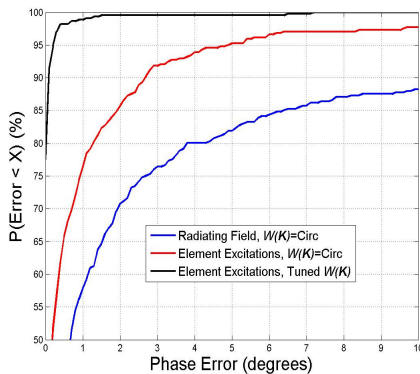


Figure 11 – Phase-Error CDFs

6. Conclusions

We have compared three methods for estimating the set of element excitations that lead to a measured SNF pattern. These methods include two traditional techniques: back-projection to the radiating aperture field, and transformation after dividing by the element pattern. We introduced an alternative technique of tuning the spectral truncation window $W(\mathbf{K})$ to improve the orthogonality of the impulse responses $w(\mathbf{R})$ over the sample set of the element locations. This new technique has been coupled with the traditional element-excitation technique to form an enhanced element-excitation method. The three methods were compared using both measured and synthesized data. In all cases, the element excitation with the tuned spectral window provided the best results.

7. References

- [1] D.W. Hess, S. McBride, An Evaluation of the Aperture Back-Projection Technique Using Measurements Made on a Flat Plate Array with a Spherical Near-Field Arch, AMTA Proceedings, Salt Lake City, pp. 192-198, 1 - 6 November, 2009.
- [2]. P.L. Ransom , R. Mittra, "A Method of Locating Defective Elements in Large Phased Arrays," Proceedings of the IEEE, pp 1029-1030, June, 1971.
- [3] P.L. Ransom, R. Mittra, "A Method of Locating Defective Elements in Large Phased Arrays," pp. 351-356, *Phased Array Antennas*, Artech House, Norwood, MA, 1972.
- [4] J.D. Hanfling, G.V. Borgiotti, L. Kaplan, "The Backward Transform of the Near-Field for Reconstruction of Aperture Fields,," IEEE AP-S Symposium Digest, Vol.2, pp 764-7671-854, 1979.
- [5] W.T. Patton, "Method of Determining Excitation of Individual Elements of a Phased Array from Near-Field Data, U.S. Patent No. 4,453,164, June 5, 1984
- [6] W.T. Patton, L.H. Yorinks, "Near-Field Alignment of Phased Array Antennas," IEEE Transactions on Antennas and Propagation, Vol., 47, No. 3., March 1999, pp.584-591.
- [7] J.J. Lee, E. Ferren, "Sidelobe Reduction by Using Near Field Backward Transform to Correct Aperture Phase Errors," IEEE AP-S Symposium Digest, Vol.2, pp 851-854, 1988.
- [8] J.J. Lee, E.M. Ferren, D.P.Woollen, K.M. Lee, Near-Field probe Used as a Diagnostic Tool to Locate Defective Elements in an Array Antenna, IEEE Transactions on Antennas and Propagation, Vol., 36, No. 3, pp. 884-889, June, 1988.
- [9] P.A. Langsford, M.J.C. Hayes, R.I Henderson, "Holographic Diagnostics of a Phased Array Antenna from Near-Field Measurements, pp. 10-32 - 10-36, AMTA Proceedings, 1989 AMTA Symposium, Monterey, CA..
- [10] D. Garneski, "New Implementation of the Planar Near-Field Back Projection Technique for Phased Array Testing and Aperture Imaging, AMTA Proceedings, pp.9-9 - 9-14, AMTA 1990 Symposium, Philadelphia, PA..
- [11] M.G. Guler, E.B. Joy, "High Resolution Spherical Microwave Holography, "IEEE Transactions on Antennas and Propagation, Vol., 43, No. 5.,May 1995 , pp. 464-472.
- [12] C. Cappellin, A. Frandsen, O.Breinbjerg, "Application of the SWE-to-PWE antenna diagnostics technique to an offset reflector antenna, *IEEE Antenna & Propagation Magazine*, Vol 50, pp.204-213, October 2008.
- [13] D.E. Dudgeon, R.M. Mersereau, *Multidimensional Digital Signal Processing*, Prentice Hall, 1984.
- [14] A.V. Oppenheim, R.W. Schaffer, *Discrete-Time Signal Processing*, pg 61, Prentice Hall, 1989.